




Article

# Ameliorative Corrosion Resistance and Microstructure Characterization of 2205 Duplex Stainless Steel by Regulating the Parameters of Pulsed Nd:YAG Laser Beam Welding

Hany S. Abdo <sup>1</sup>, Asiful H. Seikh <sup>1,\*</sup>, Jabair Ali Mohammed <sup>1</sup> and Tauriq Uzzaman <sup>2</sup>

<sup>1</sup> Mechanical Engineering Department, King Saud University, P.O. Box 800, Al-Riyadh 11421, Saudi Arabia; habdo@ksu.edu.sa (H.S.A.); jmohammed@ksu.edu.sa (J.A.M.)

<sup>2</sup> Electrical Engineering Department, King Saud University, P.O. Box 800, Al-Riyadh 11421, Saudi Arabia; uzzaman.tauriq@gmail.com

\* Correspondence: aseikh@ksu.edu.sa

**Abstract:** Welding parameters can greatly affect the final product. In this study, there was a variation given on the pulse energy, i.e., heat input parameters. The microstructure was analyzed and presented in relation to the efficiency of corrosion. The microstructural study showed the changes of the fusion zone (FZ) and the heat-affected zone (HAZ) with an increase in pulse energy. The development of a prominent austenite process on the weld material had a prolonged effect on its corrosion resistance property. Electrochemical impedance spectroscopy (EIS) and potentiodynamic measurements were used to test the electrochemical activity of laser-weld 2205 duplex stainless steel in an aqueous 3.5% NaCl solution. Finally, the findings of the EIS analysis were supported by Raman spectroscopy. Based on the obtained results, the 2205 duplex stainless steel (DSS) weld obtained at a higher pulse energy showed higher corrosion resistance than the welded sample obtained at a low pulse energy. The impedance spectroscopy confirmed a smooth surface property with an increase in the pulse energy and the presence of an oxide layer, a finding also confirmed by the Raman spectroscopy measurements.

**Keywords:** pulse energy; microstructure; potentiodynamic polarization; EIS; Raman spectroscopy



**Citation:** Abdo, H.S.; Seikh, A.H.; Mohammed, J.A.; Uzzaman, T. Ameliorative Corrosion Resistance and Microstructure Characterization of 2205 Duplex Stainless Steel by Regulating the Parameters of Pulsed Nd:YAG Laser Beam Welding. *Metals* **2021**, *11*, 1206. <https://doi.org/10.3390/met11081206>

Academic Editors: Andrei C. Popescu, Liviu Duta and Ion N. Mihailescu

Received: 29 June 2021  
Accepted: 26 July 2021  
Published: 28 July 2021

**Publisher's Note:** MDPI stays neutral with regard to jurisdictional claims in published maps and institutional affiliations.



**Copyright:** © 2021 by the authors. Licensee MDPI, Basel, Switzerland. This article is an open access article distributed under the terms and conditions of the Creative Commons Attribution (CC BY) license (<https://creativecommons.org/licenses/by/4.0/>).

## 1. Introduction

There are several advantages of using duplex stainless steel over the austenitic grades. Duplex grades are cost-effective and lightweight compared to their austenitic counterparts, though the latter possess better corrosion resistance and approximately double the yield strength in some cases. Duplex stainless steel (DSS) comprises an equivalent amount of the ferrite and austenite phases. During solidification, the duplex solidifies in ferrite mode, and the transformation of ferrite to austenite also occurs, a process which is controlled by nitrogen diffusion [1]. The austenite initially precipitates at the grain boundaries at the time of cooling, then at the Widmanstätten plates, and eventually as intergranular precipitates [2]. The duplex steel exhibits excessively ferritic microstructures with deteriorated welding metal properties during the autogenous laser welding phase [3–9], and is thus avoided. The DSS does not have sufficient time to form an austenitic phase during laser welding in the case of low heat input and rapid cooling. Solidification structures of close to 100% ferrite are noticed in DSS 2205 [8,10]. The ferrite phase precipitation of chromium nitride has a negative influence on toughness and corrosion behavior [3,11–13]. Usually, these precipitations are of the Cr<sub>2</sub>N form and can cause chromium reduction in the ferrite grain boundaries, which eventually contributes to a reduction in local pitting resistance [13–15]. The benefits of using laser welding methods for welding duplex stainless steel are high welding speed, low distortion, and gap bridge capacity. The main difference for duplex grades is the higher heat input relative to laser welding, resulting in decreased cooling rates and hence improved austenite forming [16,17].

As discussed earlier, the DSSs have good weldability, but the favorable duplex microstructure deteriorates during welding because of the presence of defects within the fusion zone (FZ) and the heat-affected zone (HAZ) of the structure; such defects are due to the melting and solidification process [18]. Heat generally is transmitted from the FZ to the HAZ while welding. The FZ and the HAZ are hence considered to be the weak points, and welding failures tend to occur in these regions. The ferrite–austenite phase ratio of DSSs must be preserved at close to 50:50 in order to obtain the required mechanical properties and corrosion resistance properties. However, this phase ratio equilibrium can be hampered by the slow/fast-cooling thermal cycles in the welding process. The rate of cooling and the transformation extent of  $\delta$ -ferrite  $\rightarrow$   $\gamma$  are controlled by the heat input during welding [19]. Primary austenite dissolution occurs initially during welding, accompanied by grain growth within the  $\delta$ -ferrite, and finally, during cooling, austenite reformation occurs. In general, at the grain boundaries, the austenite tends to nucleate, but it can also precipitate in the grain interiors at slow cooling speeds [20].

Generally, a high heat input or slow rate of cooling is favorable for austenite formation during cooling. However, the intermetallic compounds can easily be formed in the FZ and the HAZ under slow cooling rates, especially in the case of highly alloyed super duplex and hyper duplex grades [21–23]. Consequently, the corrosion resistance and toughness of the DSS decrease significantly after welding. A significant amount of ferrite phase and chromium nitride (Cr<sub>2</sub>N) particles are generated at a low heat input or during the rapid cooling process. The low solubility of nitrogen in ferrite leads to the supersaturation of nitrogen in ferrite, which leads to Cr<sub>2</sub>N precipitation after fast cooling from high temperatures [24]. In the weld region, the austenite content can be managed by regulating the Ni content in the filler material and by applying heat treatment after welding [25]. The steel compositions and welding techniques greatly influence the mechanical and corrosion-resistant properties of the welded duplex stainless steel (DSS). Several welding techniques, including laser welding, tungsten inert gas (TIG) welding, plasma arc welding, friction welding, electron beam welding, gas metal arc welding, etc., are used for the welding of DSS. All the techniques have their limitations and advantages [21,26–32]. During the welding process, variation in composition and microstructure takes place in the FZ, which may reduce the corrosion resistance of DSS. When exposed to hostile conditions, the presence of Cr<sub>2</sub>N and various intermetallic phases in welded metal will lead to low corrosion resistance [33–35]. In the present work, the effect of pulse energy on the microstructural and corrosion behavior properties of the welded DSS has been investigated.

## 2. Materials and Methods

The material used in this study was commercially available duplex stainless steel; 2205 with 4 mm plate thickness. Its chemical composition is provided in Table 1.

**Table 1.** Chemical composition of duplex 2205 (wt%).

C	Si	Mn	P	S	Al	B
0.03	0.39	1.34	0.03	<0.003	0.0039	0.0035
Cr	Cu	Mo	Ni	Nb	Co	Ti
22.5	0.24	3.03	5.6	0.016	0.128	<0.005

The laser welding was carried out using a 9000W laser power device PLDD-100M (ALPHALAS, Goettingen, Germany), a laser wavelength of 1070 nm, a pulse duration of 5 ms and a laser spot diameter of 1.5 mm on pulsed wave Nd:YAG laser mode and high-purity argon gas with a flow rate of 15 L/min during the welding process. The effect of the laser power was clarified using a fixed welding speed of 0.5 m/min and defocusing distances of  $-2.0$  mm. Three different laser powers of 4.5 kW, 6.5 kW and 8.5 kW were chosen in order to analyze the effect of laser power on the weld quality. The processing parameters are provided in Table 2.

**Table 2.** Process parameter of laser welding for joining 2205 duplex stainless steel.

Laser Power (kW)	Welding Speed (m/min)	Defocusing Distances (mm)	Shielding Gas/Flow Rate (L/min)
4.5	0.5	−2	Argon/15
6.5			
8.5			

The polishing of samples was performed using various grades (400–1500 grades) of silicon carbide emery papers; the samples were also polished with abrasives such as alumina and 0.03  $\mu\text{m}$  colloidal silica. An ultrasonic cleaner was then used to clean the specimens. By etching the polished samples using Kalling’s No. 2 (5 g copper chloride, 100 mL hydrochloric acid, and 100 mL ethanol), the microstructure of the welded joint for the overlapped sheets was analyzed. Microstructural analysis of the sample and the welded joint was examined under a Leica optical microscope DM3 XL (Leica Microsystems, Bourges, France).

The Raman spectrum of the sample was measured using a Raman spectrometer LabRAM HR800 (HORIBA Jobin Yvon, Paris, France) with an incident laser light at a wavelength of 514.5 nm. Raman bands were calibrated using the 520  $\text{cm}^{-1}$  band from Si. The Raman spectra were taken at three appropriate points on each sample in the range of 200 to 1000  $\text{cm}^{-1}$ .

A three-electrode corrosion cell was used for EIS measurements. The impedance experiments were performed in the frequency range of 0.01 Hz to 100 kHz. The absolute impedance and phase angles were measured at each frequency and the Nyquist and Bode plots were obtained. Using actual and imaginary data components in a simplex fit model, the impedance data were fitted into a suitable equivalent electrical circuit. Based on this equivalent electrical circuit, the impedance data were analyzed. Electrochemical parameters were obtained after the EIS studies from EIS curves from figure to figure. The EIS parameters are tabulated in Table 2.

The corrosion behavior of the welded material was studied in a 3.5% NaCl solution with a pH value of 7. Potentiodynamic polarization tests of all welded samples were conducted at room temperature at a scan rate of 1 mV/s using a Gamry Potentiostatic (PC/750, USA) device in the NaCl solution. The duplex stainless-steel samples were cleaned with acetone and ethanol after being polished with emery papers and cloth polishers. A standard three-electrode system was used to measure the  $i_{\text{corr}}$  and  $E_{\text{corr}}$  of the sample. A saturated calomel electrode (SCE) was used as a reference electrode with graphite taken as an auxiliary electrode; the sample was a working electrode. The surface area exposed to the solution differed from sample to sample, but it was standardized to a fixed sample area at the time of plotting. The  $i_{\text{corr}}$  and  $E_{\text{corr}}$  values obtained from the figure by the Tafel extrapolation method are tabulated in Table 3.

### 3. Results and Discussion

#### 3.1. Microstructure Analysis

The microstructure of duplex stainless steel is shown in Figure 1. From the figure, it is observed that it has a duplex steel structure, which can be attributed to the existence of ferrite and austenite phases in equal volumes. These two phases are layered and have discrete and detectable grain boundaries. The microstructure was observed using a light microscope (LM) as presented in Figure 1. The brown area depicts the phase of ferrite ( $\delta$ ), while the phase of austenite ( $\gamma$ ) is shown in black.

In the fusion zone, a dendritic microstructure was found owing to the accelerated cooling of the welded metal (Figure 2). Upon further cooling, the austenite phase formation took place at the ferrite grain boundary. A more globular shape structure was observed at the center of the welding metal due to its improper heat flow and low cooling speeds. The solidification of the DSS weld metal led to the formation of an  $\alpha$ -ferrite phase. By

managing the subsequent transformation of the solid-state phase, the volume fraction of austenite was managed [36].

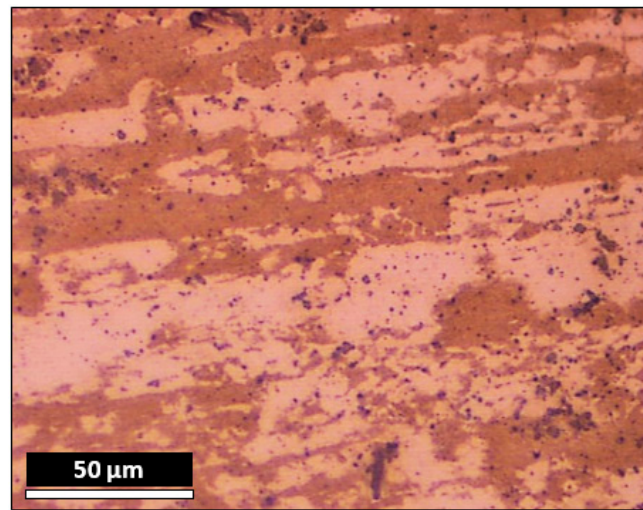


Figure 1. Microstructure of 2205 duplex stainless steel.

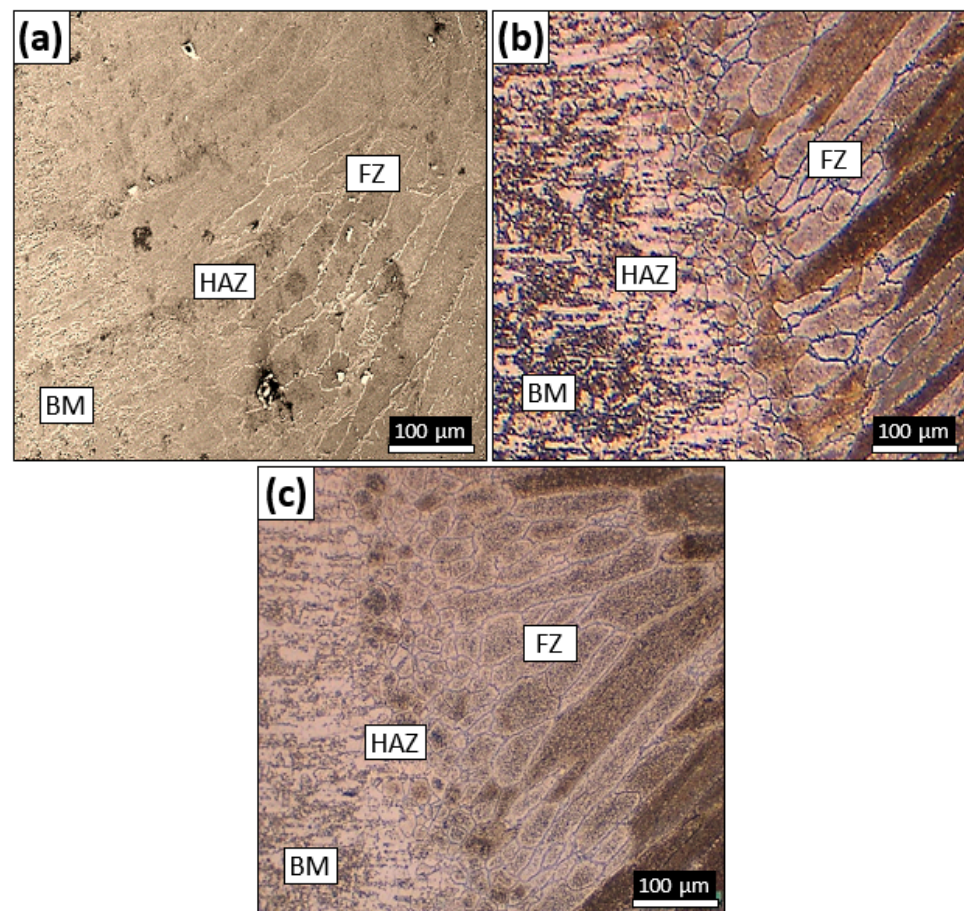
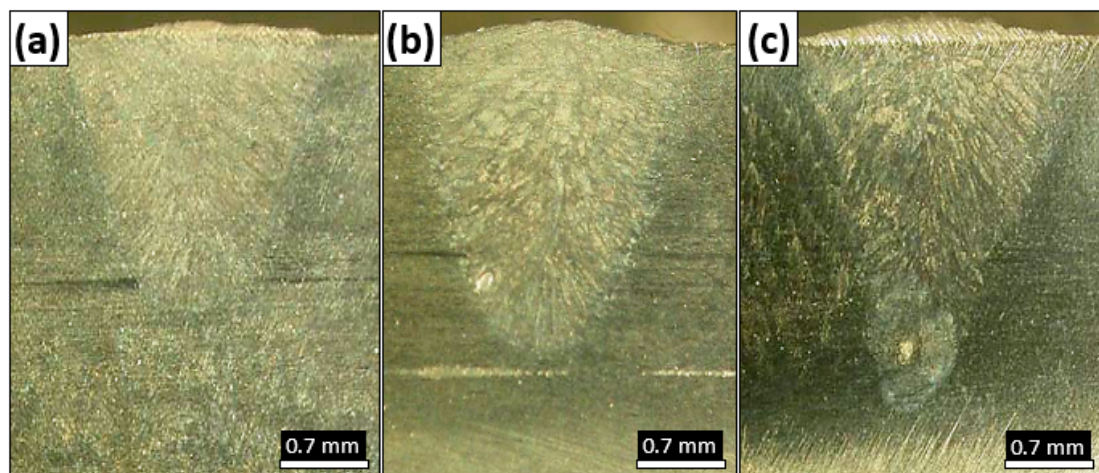


Figure 2. Optical micrographs of the laser-overlapped welded joint formed using (a) 4.5 kW; (b) 6.5 kW and (c) 8.5 kW power. [BM: base metal; HAZ: heat-affected zone; FZ: fusion zone].

The HAZ zone increased with increasing pulse energy. At the lowest energy, the HAZ zone was almost invisible. As the energy was increased, the austenite formation with a prominent grain boundary occurred in the fusion zone, and a substantial difference

was observed in the structure of the heat-affected zone (HAZ) and the fusion zone (FZ) compared to that of the base metal (BM).

As shown in Figure 3, the cross section of the laser weld sheets had a narrow and regular form and were free of any defects in solidification and shrinkage. The penetration depth increased steadily with the rise in heat supply, resulting in a complete penetration of welding and providing enhanced mechanical strength. Mirakhorli et al. [37] reported that with the heat input and overlap factor, the penetration depth increases and adversely affects the penetration depth when welding duplex stainless steel. It is, therefore, necessary to choose the right experimental conditions for the welding of duplex stainless steel. Shallow and incomplete penetration and formation of defects, such as pores and cracks, etc., may result if the experimental conditions are outside the preferred area. This would result in joints that have lower strength than the base alloy.



**Figure 3.** Macrographs of cross sections of laser sheet welds formed using a 0.5 m/min welding speed,  $-2$  mm defocusing distance, 15 L/min Argon flowrate at different pulse energies (a) 4.5 kW; (b) 6.5 kW and (c) 8.5 kW.

### 3.2. Potentiodynamic Polarization

In Table 3 and Figure 4, the effect of heat supply on the corrosion resistance of laser-welded joints of overlapped sheets is shown. It was observed that increasing the heat input improved the corrosion properties of the welded joints. This heat input effect was supported by observing the cooling rates. In laser welds at low heat supply, the rapid cooling rate resulted in chromium nitride (CrN) precipitation and an inadequate volume fraction of austenite. This effect rendered the drop-in chromium precipitation in the surroundings of the weld, which may have led to a significant impact on the corrosion resistive properties of the steel.

**Table 3.**  $E_{\text{corr}}$  and  $i_{\text{corr}}$  values of welded duplex 2205 stainless steel in 3.5% NaCl solution.

Sample Name	$E_{\text{corr}}$ (V vs. SCE)	$i_{\text{corr}}$ (A/cm <sup>2</sup> )
8.5 kW	$-0.1831$	$1 \times 10^{-7}$
6.5 kW	$-0.2339$	$6 \times 10^{-7}$
4.5 kW	$-0.3157$	$4 \times 10^{-6}$

The best corrosion resistance was therefore obtained by increasing the pulse energy, i.e., the heat input. By doing so, the surface property was also slightly improved. The microstructure showed that a higher energy input produces a smoother weld surface than the surface obtained using a lower energy input. These effects of the crevice or uneven surface, together with higher austenite levels, were eliminated, and thus the corrosion resistance was improved. After welding at higher heat input and lower cooling rates, the formation of higher austenite phases took place in the welding region. The austenitic

phase was more resistant to pitting, and hence the overall corrosion resistance property increased. Among all three samples, the sample welded at the highest pulse energy (at 8.5 kW) showed the best corrosion resistance property ( $1 \times 10^{-7} \text{ A/cm}^2$ ) as well as the highest passivity, i.e., the highest  $E_{\text{corr}}$  value compared to the other two samples.

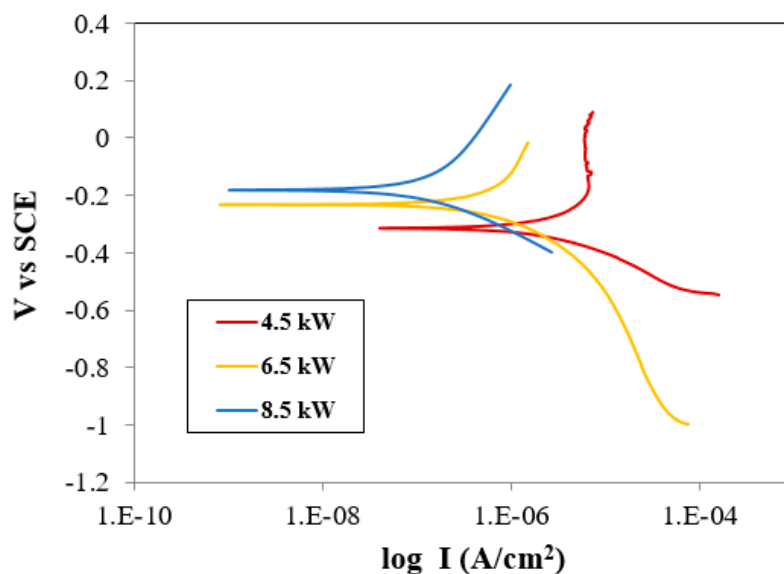


**Figure 4.** Potentiodynamic polarization diagram of 2205 duplex stainless steel welded with different pulse energy conditions.

### 3.3. Electrochemical Impedance Spectroscopy

For each of the three frequencies of 2205 duplex stainless steel, the real impedance is plotted against the imaginary impedance in Figure 5. The Nyquist graph exhibited a depressed semicircle. When welding with increased pulse energy, the diameter of the capacitive semicircle in the Nyquist plot increased. The diameter of the semicircle represents the polarization resistance of the surface. With an increase in this resistance, the corrosion resistance property of the steel also increased, a finding which is evident from the corrosion data provided in Table 3.

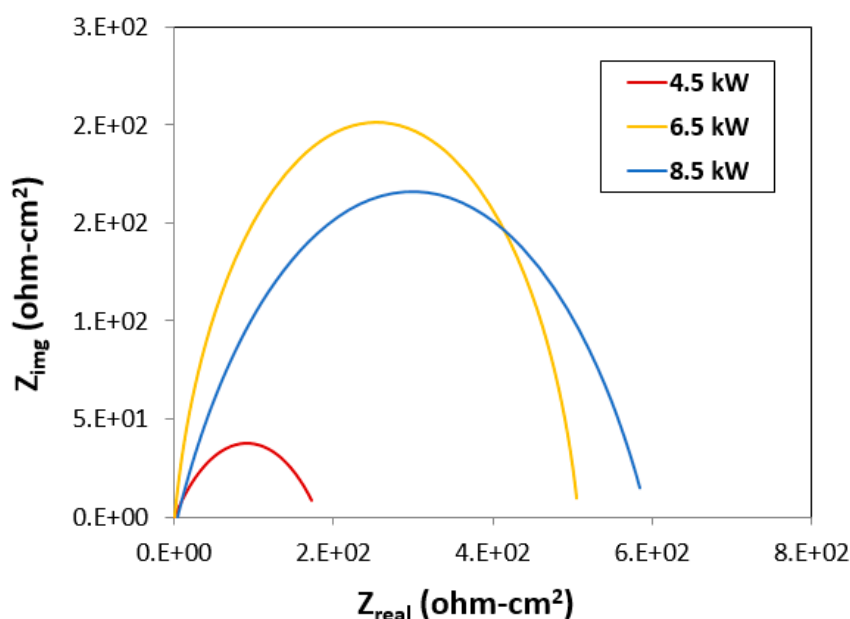


**Figure 5.** Nyquist plot of 2205 duplex stainless steel in 3.5% NaCl solution.

Bode magnitude plots and phase plots are provided in Figures 6 and 7, respectively. The bode magnitude plot clearly exhibits two distinct regions. In the low- and high-frequency regions, the graph exhibits constant  $\log |Z|$  values w.r.t  $\log (f)$ . This type indicates the response to the solution resistance [38,39]. The spectrum shows a linear slope of about  $-1$  in the wide middle frequency range (1–1000 Hz). This is the distinctive response of the surface film's capacitive actions [38,40].

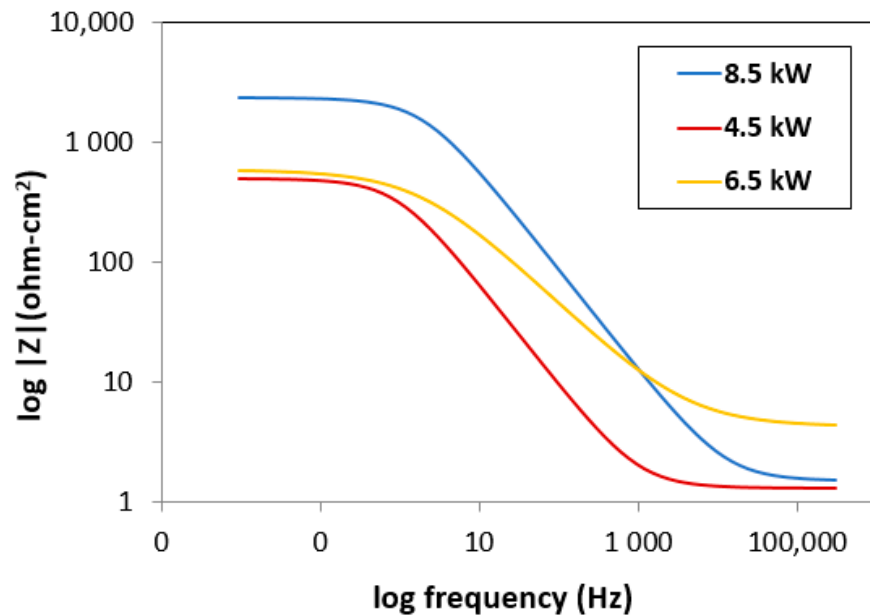


Figure 6. Bode magnitude plot of 2205 duplex stainless steel in 3.5% NaCl solution.

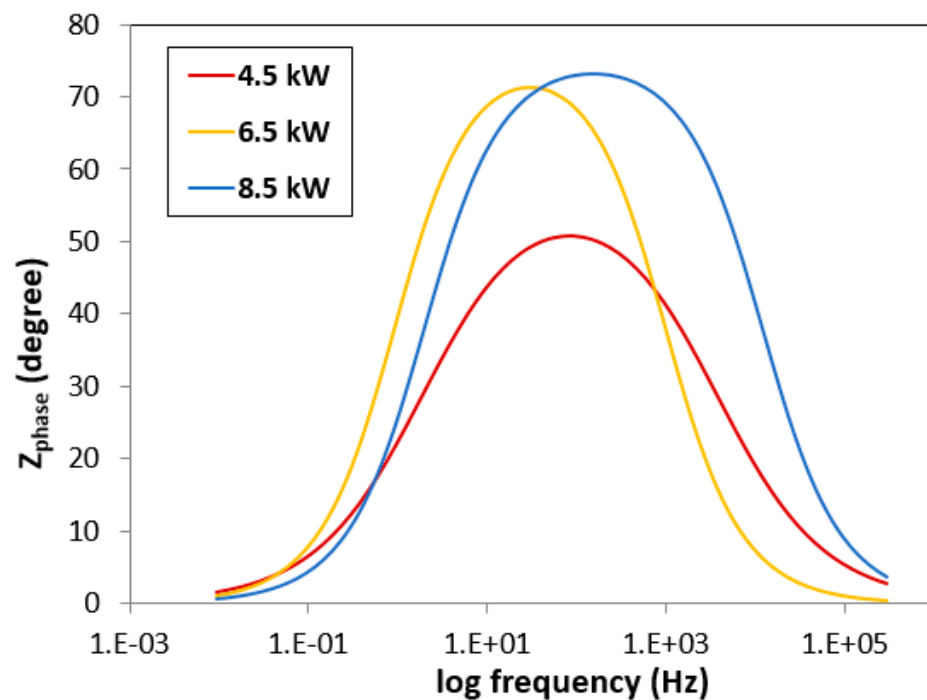
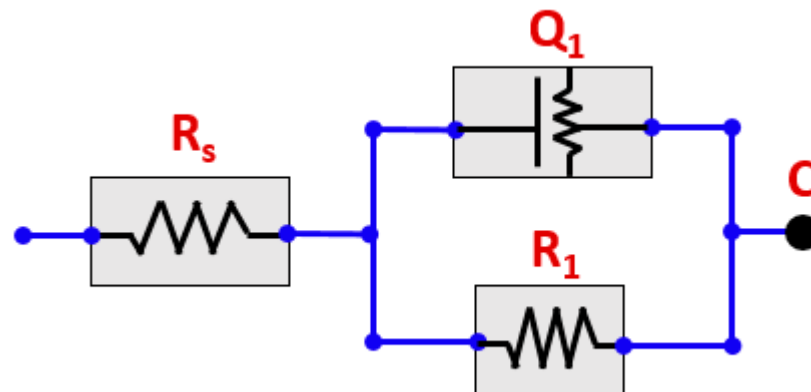


Figure 7. Bode phase plot of 2205 duplex stainless steel in 3.5% NaCl solution.

In the low-frequency region, the curve shifted to a higher modulus with increasing pulse energy or heat input. This indicates that the solution resistance increases as the pulse energy increases.

In the Bode phase plot, the phase angles of two samples (8.5 kW and 6.5 kW pulse energy) approach  $75^\circ$  at the intermediate frequency range. As for the other sample (4.5 kW), the phase angle is decreased to  $50^\circ$  which indicates diffusion on the steel surface. This diffusion affects the solution resistance which also lowers the corrosion resistance property.

In Figure 8, an equivalent circuit is proposed to be adapted to the EIS results, thus evaluating the electrochemical parameters. The constant phase aspect model was verified by all the curves. The solution resistance, the charge transfer resistance and the capacitive behavior of the passive film reflect  $R_s$ ,  $R_1$  and  $Q_1$  (constant phase angle elements), respectively, in this equivalent circuit.



**Figure 8.** Equivalent circuit diagram for EIS fitting.

The charge transfer resistance of the duplex stainless steels is given in Table 4. It is obvious that the charge transfer resistance ( $R_1$ ) of the low pulse energy sample is always lower than that of the higher pulse energy sample.

**Table 4.** EIS fitting data of 2205 DSS in 3.5% NaCl solution.

Solution	$R_s$ (ohm-cm <sup>2</sup> )	$Q_1$ (ohm <sup>-1</sup> cm <sup>-2</sup> s <sup>-n</sup> )	$R_1$ (kohm-cm <sup>2</sup> )
4.5 kW	6.67	62.81	109.7
6.5 kW	7.94	66.58	155.90
8.5 kW	8.97	71.71	211.50

The CPE behavior of the oxides on the duplex stainless steel was induced by surface distributions, which can be supported by local EIS data [41]. Interestingly, the capacitance value ( $Q_1$ ) and the passive film thickness also increases as the pulse energy input rises.

### 3.4. Raman Spectroscopy

Figure 9 show the Raman spectra of the passive film formed on the 2205 duplex stainless steels at different pulse energies. The Raman spectra display two clear broad peaks at  $365\text{ cm}^{-1}$  and  $550\text{ cm}^{-1}$  corresponding to the hematite and magnetite [42]. The presence of the high amounts of dopants or defects in magnetite as compared to hematite is the reason for the difference in the peak for magnetite [43]. It can be deduced that the passive films in 2205 duplex stainless steel with higher pulse energy will have significantly higher corrosion resistance as compared to those with lower pulse energy. The results of the Raman spectra suggest that the increase in the concentration of hematite in 2205 duplex stainless steel may lead to a decrease in the passive film point defects. It also proves that higher pulse energy increases the passive film corrosion resistance generated in 2205 DSS in an aqueous NaCl solution.



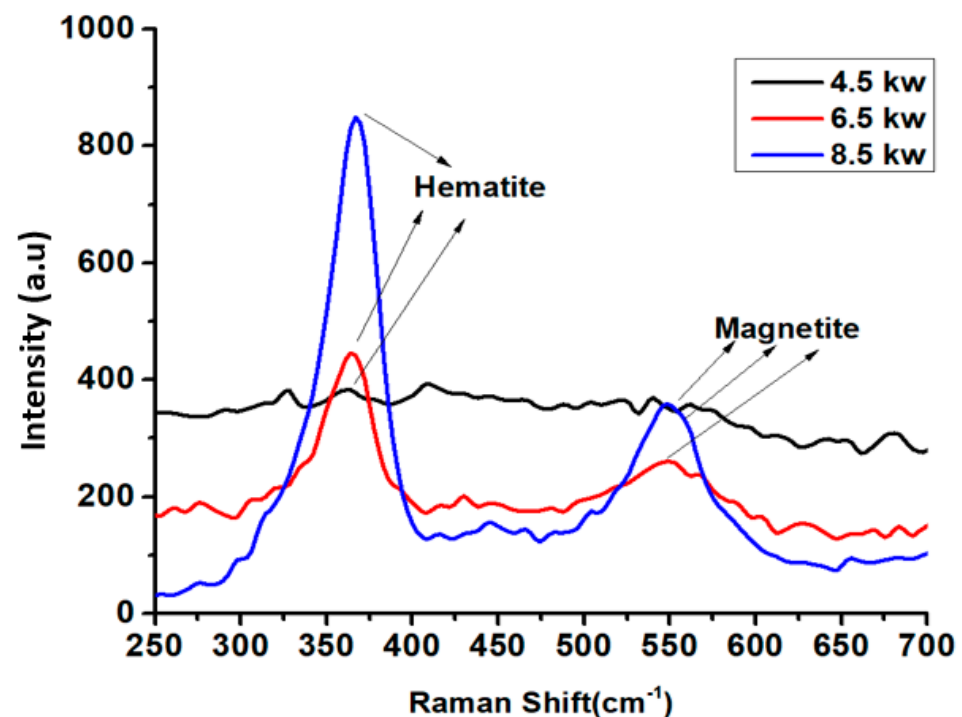


Figure 9. Raman spectra of the passive film formed at 4.5 kW, 6.5 kW and 8.5 kW on 2205 duplex stainless steels.

#### 4. Conclusions

The input parameters of the energy-pulsed Nd:YAG laser beam welding of 2205 duplex stainless steel were investigated using experimental methods. Based on the research conducted, the following qualitative and quantitative conclusions can be made:

1. By increasing laser energy, the austenite formation with a prominent grain boundary occurs in the fusion zone;
2. From the micrograph, it can be deduced that the penetration depth increases steadily with the rise in heat supply, resulting in a complete penetration of welding and providing enhanced mechanical strength;
3. The 2205 duplex stainless steel weld obtained at a higher pulse energy showed higher corrosion resistance than the welded sample obtained at a low pulse energy. The best corrosion resistance property of  $1 \times 10^{-7}$  A/cm<sup>2</sup>, as well as the highest passivity, was for the highest pulse energy value of 8.5 kW;
4. The impedance spectroscopy confirms a smooth surface property with an increase in the pulse energy and the presence of an oxide layer, a finding which is also confirmed by the Raman spectroscopy measurement.

**Author Contributions:** Conceptualization, H.S.A. and A.H.S.; methodology, H.S.A. and J.A.M.; software, T.U.; validation, H.S.A. and A.H.S.; formal analysis, J.A.M. and T.U.; investigation, H.S.A.; resources, H.S.A.; data curation, J.A.M. and T.U.; writing—original draft preparation, H.S.A.; writing—review and editing, H.S.A.; visualization, J.A.M. and T.U.; supervision, H.S.A.; project administration, A.H.S.; funding acquisition, A.H.S. All authors have read and agreed to the published version of the manuscript.

**Funding:** This research is funded by Researchers Supporting Project number (RSP-2021/373), King Saud University, Riyadh, Saudi Arabia.

**Institutional Review Board Statement:** Not applicable.

**Informed Consent Statement:** Not applicable.

**Data Availability Statement:** Not applicable.

**Acknowledgments:** The authors would like to acknowledge the Researchers Supporting Project number (RSP-2021/373), King Saud University, Riyadh, Saudi Arabia.

**Conflicts of Interest:** The authors declare no conflict of interest.

## References

1. Gooch, T.G. Corrosion Behavior of Welded Stainless Steel. In Proceedings of the Duplex Stainless Steels, Cleveland, OH, USA, 3–7 April 1996; pp. 573–602.
2. Nilsson, J.O.; Wilson, A.; Josefsson, B.; Thorvaldsson, T. Proceedings of the Applications of Stainless Steel. *Mater. Sci. Technol.* **1992**, *8*, 685–700. [[CrossRef](#)]
3. Lv, J.; Jin, H.; Liang, T. The Effect of Electrochemical Nitridation on the Corrosion Resistance of the Passive Films Formed on the 2205 Duplex Stainless Steel. *Mater. Lett.* **2019**, *256*, 126640.
4. Abdo, H.S.; Sarkar, A.; Gupta, M.; Sahoo, S.; Mohammed, J.A.; Ragab, S.A.; Seikh, A.H. Low-Cost High-Performance SnO<sub>2</sub>-Cu Electrodes for Use in Direct Ethanol Fuel Cells. *Crystals* **2021**, *11*, 55. [[CrossRef](#)]
5. Hoffmeister, H.; Lothongkum, G. Quantitative effects of nitrogen contents and cooling cycles on  $\delta$ - $\gamma$  transformation, chromium nitride precipitation and pitting corrosion after weld simulation of duplex stainless steels. In Proceedings of the Forth International Conference on Duplex Stainless Steels, Glasgow, UK, 13–16 November 1994; p. 55.
6. Abdo, H.S.; Seikh, A.H.; Mandal, B.B.; Mohammed, J.A.; Ragab, S.A.; Abdo, M.S. Microstructural Characterization and Corrosion-Resistance Behavior of Dual-Phase Steels Compared to Conventional Rebar. *Crystals* **2020**, *10*, 1068. [[CrossRef](#)]
7. Yin, L.; Xu, D.; Yang, C.; Xi, T.; Chen, X.; Yang, K. Ce Addition Enhances the Microbially Induced Corrosion Resistance of Cu-bearing 2205 Duplex Stainless Steel in Presence of Sulfate Reducing Bacteria. *Corros. Sci.* **2021**, *179*, 109141. [[CrossRef](#)]
8. Abdo, H.S.; Seikh, A.H.; Mohammed, J.A.; Luqman, M.; Ragab, S.A.; Almotairy, S.M. Influence of Chloride ions on Electrochemical Corrosion Behavior of Dual-phase Steel over Conventional Rebar in Pore Solution. *Appl. Sci.* **2020**, *10*, 4568. [[CrossRef](#)]
9. Liu, D.; Jia, R.; Xu, D.; Yang, H.; Zhao, Y.; Khan, M.; Huang, S.; Wen, J.; Yang, K.; Gu, T. Biofilm Inhibition and Corrosion Resistance of 2205-Cu Duplex Stainless Steel against Acid Producing Bacterium *Acetobacter aceti*. *J. Mater. Sci. Technol.* **2019**, *35*, 2494–2502. [[CrossRef](#)]
10. Abdo, H.S.; Seikh, A.H.; Fouly, A.; Ragab, S.A. Synergistic Strengthening Effect of Reinforcing Spark Plasma Sintered Al-Zn-TiC Nanocomposites with TiC Nanoparticles. *Crystals* **2021**, *11*, 842. [[CrossRef](#)]
11. Liou, H.Y.; Hsieh, R.I.; Tsai, W.T. Microstructure and Stress Corrosion Cracking in Simulated Heat-affected Zones of Duplex Stainless Steels. *Corros. Sci.* **2002**, *44*, 2841–2856. [[CrossRef](#)]
12. Kwok, C.T.; Fong, S.L.; Cheng, F.T.; Man, H.C. Pitting and Galvanic Corrosion Behaviour of Laser-welded Stainless Steels. *J. Mater. Process. Technol.* **2006**, *176*, 168–178. [[CrossRef](#)]
13. Pettersson, R.J. The influence of microstructure on pitting corrosion in autogenous TIG duplex stainless steel welds. In Proceedings of the Duplex Stainless Steels, Glasgow, UK, 13–16 November 1994; pp. 461–472.
14. Sridhar, N.; Kolts, J. Effects of Nitrogen on the Selective Dissolution of a Duplex Stainless Steel. *Corrosion* **1987**, *43*, 646–651. [[CrossRef](#)]
15. Abdo, H.S.; Seikh, A.H.; Mohammed, J.A.; Soliman, M.S. Alloying Elements Effects on Electrical Conductivity and Mechanical Properties of Newly Fabricated Al Based Alloys Produced by Conventional Casting Process. *Materials* **2021**, *14*, 3971. [[CrossRef](#)]
16. Westin, E.M.; Keehan, E.; Ström, M.; Von Brömssen, B. Laser welding of a lean duplex stainless steel. In Proceedings of the ICALEO, Orlando, FL, USA, 29 October–1 November 2007; pp. 335–344.
17. Westin, E.M. Corrosion resistance of welded lean duplex stainless steel. In Proceedings of the Stainless Steel World America 2008, Houston, TX, USA, 9–10 September 2008; p. 17.
18. Nowacki, J.; Rybicki, P. The Influence of Welding Heat Input on Submerged Arc Welded Duplex Steel Joints Imperfections. *J. Mater. Proc. Technol.* **2005**, *164–165*, 1082–1088. [[CrossRef](#)]
19. Baeslack, W.A., III; Lippold, J.C. Phase Transformation Behavior in Duplex Stainless Steel Weldments. *Met. Constr.* **1988**, *20*, 26R–31R.
20. Seurin, H.; Sandstrom, R. Austenite Reformation in the Heat-affected Zone of Duplex Stainless Steel 2205. *Mater. Sci. Eng. A* **2006**, *418*, 250–256. [[CrossRef](#)]
21. Sasikumar, C.; Sundaresan, R.; Medona, C.M.; Ramakrishnan, A. Corrosion Study on AA-TIG Welding of Duplex Stainless Steel. *Mater. Today* **2021**, *45*, 3383–3385.
22. Chinthaka, M.S.; Leonard, K.J.; Garrison, L.M.; Bryan, C.D. Effects of Low-temperature Neutron Irradiation on the Microstructure and Tensile Properties of Duplex 2304 Stainless Steel and Its Electron-Beam Welds. *Mater. Sci. Eng. A* **2021**, *823*, 141780.
23. Wan, Y.; Jiang, W.; Wei, W.; Xie, X.; Song, M.; Xu, G.; Xie, X.; Zhai, X. Characterization of inhomogeneous microstructure and mechanical property in an ultra-thick duplex stainless steel welding joint. *Mater. Sci. Eng. A* **2021**, *822*, 141640. [[CrossRef](#)]
24. Muthupandi, V.; Srinivasan, P.B.; Sundaresan, S. Effect of Weld Chemistry and Heat Input on the Structure and Properties of Duplex Stainless Steel Welds. *Mater. Sci. Eng. A* **2003**, *358*, 9–16. [[CrossRef](#)]
25. Munoz, A.I.; Anton, J.G.; Guinon, J.L.; Herranz, V.P. Effect of Nitrogen in Argon as a Shielding Gas on TIG Welds of Duplex Stainless Steels. *Corrosion* **2005**, *61*, 693–705. [[CrossRef](#)]
26. Maurya, A.K.; Pandey, C.; Chhibber, R. Dissimilar Welding of Duplex Stainless Steel with Ni Alloys: A review. *Int. J. Press. Vessels Pip.* **2021**, *192*, 104439. [[CrossRef](#)]

27. Park, H.; Moon, B.; Moon, Y.; Kang, N. Hydrogen Stress Cracking Behaviour in Dissimilar Welded Joints of Duplex Stainless Steel and Carbon Steel. *Metals* **2021**, *11*, 1039. [[CrossRef](#)]
28. Omiogbemi, I.M.B.; Pandey, S.; Yawas, D.S.; Afolayan, M.O.; Dauda, E.T. Effect of Welding Conditions and Flux Compositions on the Metallurgy of Welded Duplex Stainless Steel. *Mater. Today* **2021**. [[CrossRef](#)]
29. Calderon-Uriszar-Aldaca, I.; Briz, E.; Garcia, H.; Matanza, A. The Weldability of Duplex Stainless-Steel in Structural Components to Withstand Corrosive Marine Environments. *Metals* **2020**, *10*, 1475. [[CrossRef](#)]
30. Chen, X.; Inao, D.; Tanaka, S.; Mori, A.; Li, X.; Hokamoto, K. Explosive Welding of Al Alloys and High Strength Duplex Stainless Steel by Controlling Energetic Conditions. *J. Manuf. Process.* **2020**, *58*, 1318–1333. [[CrossRef](#)]
31. Cui, S.; Pang, S.; Pang, D.; Zhang, Z. Influence of Welding Speeds on the Morphology, Mechanical Properties, and Microstructure of 2205 DSS Welded Joint by K-TIG Welding. *Materials* **2021**, *14*, 3426. [[CrossRef](#)] [[PubMed](#)]
32. Gao, S.; Geng, S.; Jiang, P.; Mi, G.; Han, C.; Ren, L. Numerical Analysis of the Deformation Behavior of 2205 Duplex Stainless Steel TIG Weld Joint Based on the Microstructure and Micro-mechanical Properties, *Mater. Sci. Eng. A* **2021**, *815*, 141303. [[CrossRef](#)]
33. Zhang, Z.; Wang, Z.; Jiang, Y.; Tan, H.; Han, D.; Guo, Y. Effect of Post-weld Heat Treatment on Microstructure Evolution and Pitting Corrosion Behavior of UNS S31803 Duplex Stainless Steel Welds. *Corros. Sci.* **2012**, *62*, 42–50. [[CrossRef](#)]
34. Turnbull, A.; Francis, P.E.; Ryan, M.P.; Orkney, L.P.; Griffith, A.J.; Hawkins, B. A Novel Approach to Characterizing Corrosion Resistance of Super Duplex Stainless Steel Weld. *Corrosion* **2002**, *58*, 1039–1048. [[CrossRef](#)]
35. Nilsson, J.O. Overview of Super Duplex Stainless Steel. *Mater. Sci. Technol.* **1992**, *8*, 685–700. [[CrossRef](#)]
36. Nowacki, J.; Lukojc, A. Microstructural Transformations of Heat Affected Zones in Duplex Steel Welded Joints. *Mater. Charact.* **2006**, *56*, 436–441. [[CrossRef](#)]
37. Mirakhorli, F.; Ghaini, F.M.; Torkamany, M.J. Development of Weld Metal Microstructures in Pulsed Laser Welding of Duplex Stainless Steel. *J. Mater. Eng. Perform.* **2012**, *21*, 2173–2176. [[CrossRef](#)]
38. Loveday, D.; Peterson, P.; Rodgers, B. Evaluation of Organic Coatings with Electrochemical Impedance Spectroscopy. *JCT Coat. Tech.* **2004**, *8*, 46–52.
39. Shukla, A.K.; Balasubramaniam, R.; Bhargava, S. Properties of Passive Film Formed on CP Titanium, Ti-6Al-4V and Ti-13.4Al-29Nb Alloys in Simulated Human Body Conditions. *Intermetallics* **2005**, *13*, 631–637.
40. Kobayashi, E.; Wang, T.J.; Doi, H.; Yoneyama, T.; Hamanaka, H. Mechanical Properties and Corrosion Resistance of Ti-6Al-7Nb Alloy Dental Castings. *J. Mater. Sci. Mater. Med.* **1998**, *9*, 567–574. [[CrossRef](#)] [[PubMed](#)]
41. Huang, V.M.W.; Vivier, V.; Frateur, I.; Orazem, M.E.; Tribollet, B. The Global and Local Impedance Response of a Blocking Disk Electrode with Local Constant-phase-element Behavior. *J. Electrochem. Soc.* **2006**, *154*, C89–C98. [[CrossRef](#)]
42. Yeh, T.K.; Chien, Y.C.; Wang, B.Y.; Tsai, C.H. Electrochemical Characteristics of Zirconium Oxide Treated Type 304 Stainless Steels of Different Surface Oxide Structures in High Temperature Water. *Corros. Sci.* **2008**, *50*, 2327–2337. [[CrossRef](#)]
43. Cornell, R.M.; Schwertmann, U. *The Iron Oxides: Structure, Properties, Reactions, Occurrences and Uses*, 2nd ed.; John Wiley & Sons: Weinheim, Germany, 2003.